



Journal of Geophysical Research: Atmospheres

RESEARCH ARTICLE

10.1029/2018JD029180

Kev Points:

- Most of the North Pacific AR events originate in the subtropics and terminate in higher latitudes including western North America
- Long AR events travel 7 times longer in distance and have stronger intensity than short AR events
- An accumulated AR intensity index is developed to summarize the overall impact of AR events

Correspondence to:

H. Kim, hyemi.kim@stonybrook.edu

Citation:

Zhou, Y., Kim, H., & Guan, B. (2018). Life cycle of atmospheric rivers: Identification and climatological characteristics. *Journal of Geophysical Research: Atmospheres*, 123, 12,715–12,725. https://doi.org/10.1029/2018/D029180

Received 14 JUN 2018 Accepted 22 OCT 2018 Accepted article online 24 OCT 2018 Published online 28 NOV 2018

Author Contributions:

Conceptualization: Yang Zhou, Hyemi Kim, Bin Guan Formal analysis: Yang Zhou Funding acquisition: Hyemi Kim Investigation: Yang Zhou Methodology: Yang Zhou, Bin Guan Supervision: Hyemi Kim, Bin Guan Validation: Yang Zhou Visualization: Yang Zhou

Writing - original draft: Yang Zhou, Hyemi Kim

Writing – review & editing: Hyemi Kim, Bin Guan

Life Cycle of Atmospheric Rivers: Identification and Climatological Characteristics

Yang Zhou¹ , Hyemi Kim¹ , and Bin Guan^{2,3}

¹School of Marine and Atmospheric Sciences, Stony Brook University, Stony Brook, NY, USA, ²Joint Institute for Regional Earth System Science and Engineering, University of California, Los AngelesCA, USA, ³Jet Propulsion Laboratory, California Institute of Technology, Pasadena, CA, USA

Abstract An atmospheric river (AR) event is a strong poleward moisture transport that is composed of a series of spatiotemporally connected instantaneous AR objects. A new object-based tracking algorithm is developed in this study, which aims to identify an AR event and investigate its life cycle from origin to termination. The algorithm identifies duration, intensity, propagation speed and direction, and the traveled distance throughout the life cycle of the AR event. The tracking algorithm is applied to 6-hourly column-integrated water vapor flux from November to March during the period of 1979–2017, with a focus on the North Pacific. Most North Pacific AR events originate in the subtropics over the Northwest Pacific and terminate at higher latitudes over the Northeast Pacific including western North America. On average, long AR events that last more than 72 hrs travel 7 times longer in distance and have stronger intensity than short AR events that last less than 24 hrs. Finally, a new accumulated AR intensity index is developed, which summarizes the overall impact of AR events over a given domain during a certain period by incorporating number, lifetime, and intensities of AR events.

Plain Language Summary Atmospheric rivers (ARs) are "rivers" in the sky that transport water vapor from the tropics to higher latitudes. ARs play an important role in water resources because they transport as much water as the largest rivers on the ground and can often induce extreme precipitation when making landfall. A technique is developed to numerically detect and track ARs as they propagate in time and space. Based on this technique, we study the climatological characteristics of the life cycle (i.e., from appearance to disappearance) of winter ARs over the North Pacific. Most of the ARs originate at about 25°N over the Northwest Pacific and terminate between 50°N and 60°N over the Northeast Pacific. We also found that longer-lived ARs can travel 7 seven times longer distances compared to shorter-lived ARs. Finally, an index is developed to represent the overall activity of ARs of a given time period.

1. Introduction

Atmospheric rivers (ARs) are narrow plumes of intense water vapor transport with filamentary structure, which are responsible for over 90% of the poleward moisture transport while only taking up about 10% of Earth's circumference (Zhu & Newell, 1994, 1998). ARs play an important role in global hydrology and energy cycles. Typical ARs are 3,000–4,000 km long and 500–600 km wide (Guan & Waliser, 2015) while having a flow rate of water vapor (in terms of mass flux) roughly equivalent to 2.6 Amazon Rivers or 27 Mississippi Rivers (Ralph et al., 2017). ARs are synoptic phenomena that are usually associated with extra-tropical cyclones (Bao et al., 2006). ARs can relieve preexisting droughts because they usually induce precipitation in coastal regions at landfall (Dettinger, 2013). Approximately 30–50% of precipitation and snow water equivalent over the west coast of United States are attributed to landfalling ARs (Dettinger et al., 2011; Guan et al., 2010, 2013). On the other hand, coastal landmass during active AR season is at the risk of experiencing disastrous events like floodings, extreme winds, and precipitations (Bao et al., 2006; Guan & Waliser, 2017; Neiman et al., 2008; Neiman et al., 2013; Ralph et al., 2006; Waliser & Guan, 2017).

To detect ARs, one of the fundamental approaches is "condition" parameter detection, which is to identify the time step where AR conditions are met (Shields et al., 2018). The most frequently used detection parameter is the column-integrated water vapor transport (IVT; Zhu & Newell, 1998), which is calculated as

©2018. American Geophysical Union. All Rights Reserved.

$$IVT = \sqrt{\left(-\frac{1}{g}\int_{1000}^{300}qudp\right)^{2} + \left(-\frac{1}{g}\int_{1000}^{300}qvdp\right)^{2}},$$
 (1)

where g is gravitational acceleration (m s⁻²), p is pressure (hPa), q is specific humidity (kg kg⁻¹), and u and v are zonal and meridional wind vector (m s⁻¹), respectively. A variety of AR detection methods have been developed for different uses (Shields et al., 2018). For example, to detect in-land penetrating ARs, Rutz et al. (2014) defined a threshold with IVT exceeding 250 kg m $^{-1}$ s $^{-1}$ and the length being longer than 2,000 km. To study ARs globally, Guan and Waliser (2015) (hereafter, GW15) used multiple parameters including IVT, geometric shape, and directions of IVT components. If the given set of AR conditions is met, an enclosed two-dimensional (longitude and latitude) instantaneous area of strong IVT is defined as an AR object. The AR frequency is conventionally defined as the grid-point accumulated number of such AR objects over a certain period. Variability and predictability of AR frequency from subseasonal to seasonal time scales have been widely studied (Baggett et al., 2017; DeFlorio, Waliser, Guan, Lavers et al., 2018; DeFlorio, Waliser, Guan, Ralph et al., 2018; Guan & Waliser, 2015; Kim et al., 2017; Mundhenk, Barnes, Maloney, 2016; Mundhenk, Barnes, Maloney, Nardi, 2016; Mundhenk et al., 2018; Payne & Magnusdottir, 2014; Zhou & Kim, 2017). Alternatively, numerous studies investigate the temporal transportation of moisture related to ARs via the Lagrangian trajectory model. Given AR conditions, the Lagrangian model calculates the trajectories and moisture contents of single-layer air parcels within specific AR objects backward or forward in time (Bao et al., 2006; Knippertz & Wernli, 2010; Neiman et al., 2013; Ramos et al., 2016; Rutz et al., 2015; Ryoo et al., 2015; Sodemann & Stohl, 2013; Stohl et al., 2008; Stohl & James, 2004).

Another approach to detecting ARs is a "tracking" method, which considers AR objects trackable in space and time (Shields et al., 2018). AR tracking methods utilize the spatial connection between AR objects of consecutive time steps. Here we define an AR event in three dimensions (longitude, latitude, and time) as a series of spatiotemporally connected AR objects. The AR object refers to an instant snapshot of the AR event. In this study, the AR life cycle represents the spatiotemporal evolution of AR objects within an AR event. Previous studies examined the origins and terminations of extreme AR events (IVT > 750 kg m⁻¹ s⁻¹) and their responses to climate variability (Sellars et al., 2015; Sellars et al., 2017). Payne and Magnusdottir (2014, 2016) developed a semiautomated algorithm to track persistent AR events landfalling over U.S. West Coast. These studies are focused on the subsets of AR events that exceed a certain criterion of intensity, lifetime, or location. To understand the long-term climatological characteristics (origin and termination, intensity, lifetime, track, traveled distance, and propagation speed) of AR events over the entire North Pacific, a new tracking algorithm is developed. We further develop a new accumulated AR intensity (ARI) index that represents the overall activity of AR events during a certain period. The tracking algorithm is introduced in section 2. Climatological characteristics of AR life cycles and the ARI index are discussed in section 3. Summary and discussion are provided in section 4.

2. Data and Methods

2.1. Data

We employed IVT to detect AR objects. To calculate IVT, 20 vertical levels (1,000 hPa–300 hPa) of 1° longitude and latitude 6-hourly horizontal winds and specific humidity are retrieved from the European Centre for Medium-Range Weather Forecasts Interim Reanalysis (ERA-Interim; Dee et al., 2011). 6-hourly temporal resolution is the common denominator between all global reanalysis products, which is also the resolution currently adopted for archiving many climate model simulations (e.g., Guan & Waliser, 2017). The analysis season covers from November to March of 1979/1980 to 2016/2017, which is the relatively high AR landfall season in U.S. West Coast (Mundhenk, Barnes, Maloney, 2016). Hereafter, 2016/2017 winter, for example, represents all time steps between November 2016 and March 2017. In this study, we only focus on the AR events over the North Pacific (0°N–90°N, 120°E–100°W).

Following GW15, we detect AR object as a contiguous region of enhanced IVT relative to background transport. This detection method successively applies the following limits to IVT field: (i) IVT exceeds the 85th percentile or 100 kg m $^{-1}$ s $^{-1}$, whichever is greater; (ii) IVT directions are consistent among the grids and the mean IVT matches the AR object's elongated orientation; (iii) the mean IVT displays a poleward direction; and (iv) the detected AR object is spatially longer than 2,000 km, and the length-width ratio exceeds 2.

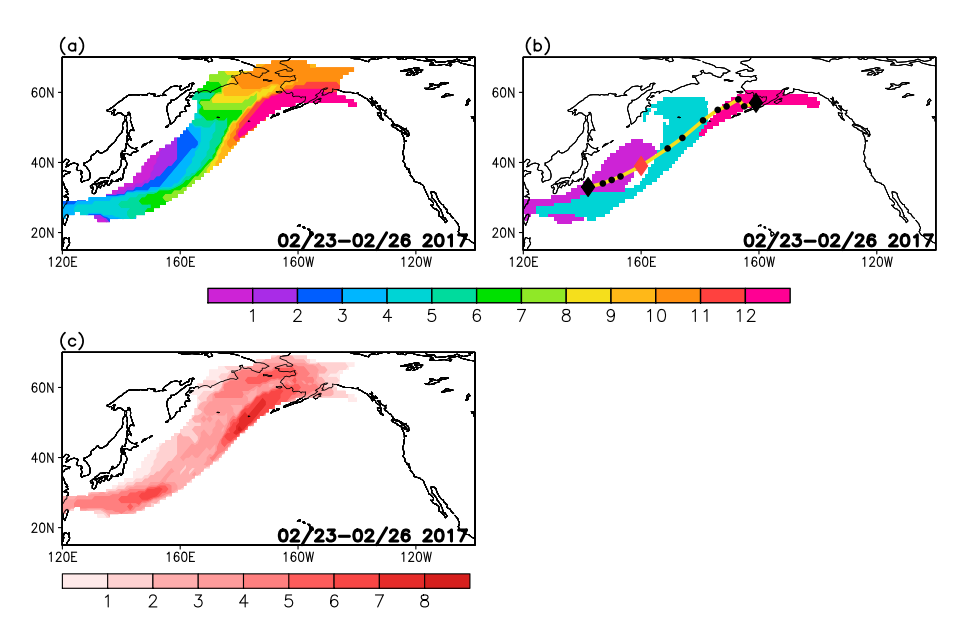


Figure 1. (a) Overlaying atmospheric river (AR) objects in the AR event during 23–26 February 2017. AR objects are marked with different colors representing consecutive time steps. (b) Selected time steps including the origin (purple), middle (blue), and termination (magenta). The black dots indicate the positions of integrated water vapor transport centroid at each time step; the black diamonds denote the origin and termination positions; the red diamond marks the position of the fifth time step. The yellow line represents the AR track. (c) Corresponding AR frequency distribution (number per grid) of the AR event shown in (a).

2.2. Tracking Algorithm

Figure 1a shows the example of an identified AR event from the tracking algorithm. This AR event lasted for 72 hrs between 23 and 26 February 2017, which contains thirteen 6-hourly time steps with overlapping AR objects. The life cycle of this AR event shows the imprints of the northeastward propagation of moisture (Figure 1a). The initial AR object (purple shading, Figures 1a and 1b) in this AR event indicates when and where this AR event first appeared, and the last AR object (magenta shading) shows when and where it terminated. For example, this AR event originated near Japan and terminated near Alaska. The positions of AR objects (dots, Figure 1b) indicate the propagation direction of this AR event. The propagation track (yellow line, Figure 1b) connects the dots (more details later).

The AR frequency, which has been frequently used in previous studies, and the AR life cycle are different perspectives of an AR event. The AR frequency shows the potential local influence of an AR event from a Eulerian perspective, and the AR life cycle represents the spatial and temporal evolution of an AR event from a Lagrangian perspective. To compare the two perspectives, we calculate AR frequency of the same AR event (Figure 1c). The AR frequency represents the accumulated number of AR objects at each grid point. As shown in Figure 1c, the magnitude of AR frequency varies among the grids. Some grids show higher frequency (like the regions near Japan and Alaska in Figure 1c) because AR conditions persist longer on these grids. However, when considering multiple AR events, high AR frequency may be attributed to multiple AR events or a single persisting AR event (Figure 1a).

Figure 2 shows the flowchart of the tracking algorithm and corresponding output. First, AR objects are detected from the IVT field using GW15 detection method. Note that AR objects from other detection methods are also suitable for our tracking algorithm. Step I of the tracking algorithm is to select the origins of AR events from the detected AR objects. The origins are classified into four types. With the selected origins, we can track the life cycles by recording the propagation track, lifetime, intensity, traveled distance, and propagation speed (Step II). A detailed explanation of each step of the tracking algorithm follows.

2.2.1. Step I: Selection of Origins

As mentioned previously, AR objects in adjacent time steps tend to overlap with each other in the same AR event. We mark the AR object from the first time step, which has no overlap with any AR objects from the

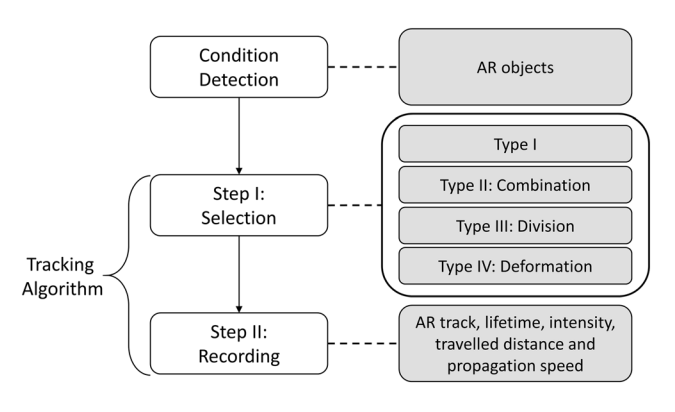


Figure 2. Schematic of the tracking algorithm and corresponding output (gray boxes).

preceding time step, as the origin of an AR event. The AR origin in Figure 1 a shows the simplest case and will be referred to as type I origin (other types are defined later). To define the origin, the overlapping ratio of AR object at time step t (AR_t) is calculated as

Overlapping ratio of
$$AR_t = \frac{Overlapping \ grids \ of \ AR_t with \ AR_{t-1}}{Total \ grids \ of \ AR_t} \times 100\%,$$
 (2)

which is the grid point ratio of AR_t 's overlapping grids with its preceding AR_{t-1} (6 hrs earlier) to the total grids of AR_t . Figure 3a shows the schematic of the calculation, which is the overlapping area (marked in yellow) of AR_t with AR_{t-1} divided by the total area of AR_t (yellow area plus blue area). Figure 3b shows 38-winter averaged distribution of overlapping ratios, which includes all detected AR objects over the North

Pacific. On average, 1,271 instantaneous AR objects (using 6-hourly data) are detected each season. Each bin includes the right edge but not the left edge except for the leftmost bin (filled in red), which represents the number of AR objects having exactly 0% overlapping ratio with its previous time step. On average, 69% of AR $_t$ have higher overlapping ratio than 50% with AR $_t$ – 1, indicating that the spatial connection between consecutive time steps within one AR event is high within the 6-hourly time interval of the data set. The wide distribution of overlapping ratios could result from (but not limited to) various propagation speeds of AR objects, since faster propagation speed could result in smaller overlapping ratio, or deformation of an AR object over its lifetime. On average, 19% (244 counts) of the total AR objects have no spatial connection with its previous time step (red bin, Figure 3b). We define these AR objects as type I origins of AR events.

The shape and number of instantaneous AR objects can change between time steps, even in the middle of the same AR event. Some AR objects may combine into one object (combination, Figure 4), while one object can divide into several smaller ones (division, Figure 4). Although these AR objects overlap with

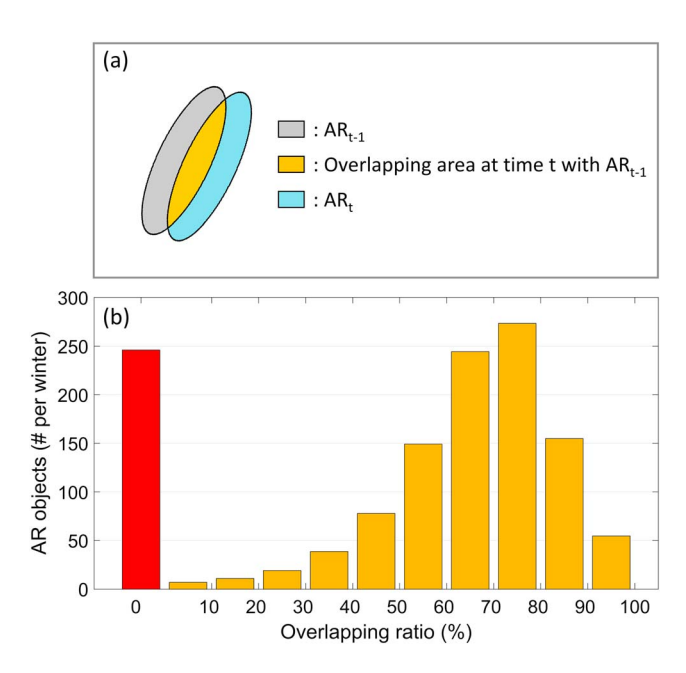


Figure 3. (a) Schematic of the calculation of overlapping ratio. (b) The number of North Pacific atmospheric river (AR) objects based on the overlapping ratio. The leftmost bin (filled in red) marks the number of AR objects with exactly 0% overlapping ratio.

previous steps (overlapping ratio >0%), the changing number of AR objects in one event complicates the definition of origin and termination. Besides, some AR objects can experience abrupt changes in shape (deformation, Figure 4), which occurs as expanding or shrinking in the spatial grids between time steps. The deformation of AR objects may break the geometrical consistency in the same AR event.

To distinguish these AR objects with inconsistent number or shape, we mark these AR objects after the changes in number or shape as origins of type II (combination), type III (division), and type IV (deformation; the blue ellipses in Figure 4). The multiple origins of type III are marked and tracked separately. The type IV origin specifically refers to deformation of a single AR object, that is, no changes in the number before and after the deformation.

Figure 4 shows the schematics of the computational selection of origins (Step I). Type I origin at t is selected when AR_t has zero overlap with the preceding time step t-1 (Figure 4). The type I origins are excluded from the iterations for type II/III/IV origins. The combination (division) decreases (increases) the number of involved AR objects. Therefore, we count the number of overlapping AR objects at neighboring time steps during the iteration. The type II origin at t is selected when it overlaps (overlapping ratio > 0%) with two or more AR objects at t-1 (Figure 4). Similarly, we can select the type III origins at t when AR_{t-1} overlaps with two or more AR objects at t. A type IV origin corresponds to the shape deformation such as expanding or shrinking. Thus, the type IV origin at t is defined when the

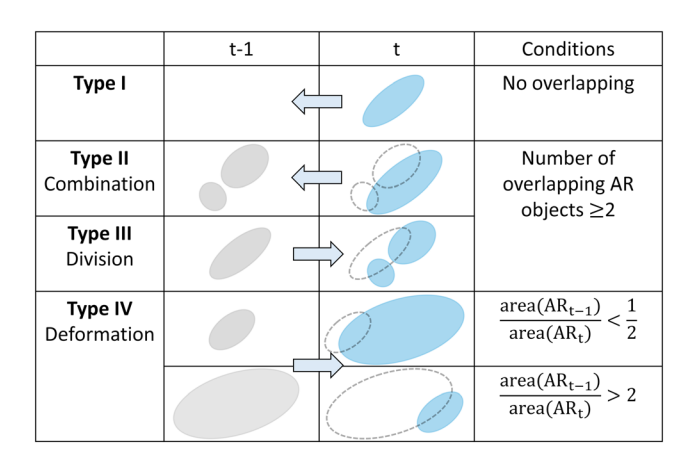


Figure 4. The selection of origin types. The arrows mark the iteration order. The blue ellipses denote the defined origins.

ratio of the area between AR_{t-1} and AR_{t} is less than 1/2 (expanding) or larger than 2 (shrinking).

In summary, the iteration first proceeds backward in time from the event termination (through the comparison of t and t-1) in order to find type I and type II origins; then it proceeds forward in time (through comparison of t-1 and t) in order to find type III and IV origins (Figure 4). The average number of AR events during each winter over the North Pacific is 102 and 73% start with type I, 8% with type II, 11% with type III, and 8% with type IV origins.

2.2.2. Step II: Recording the Life Cycle of an AR Event

Figure 5 illustrates the AR life cycle defined by the tracking algorithm. Once the origins are selected by Step I, the iteration to track the life cycle of AR events proceeds as follows: (i) Start from origin at t and record the overlapping AR object at t+1; (ii) continue with AR $_{t+1}$ and record the overlapping AR $_{t+2}$; and (iii) repeat (ii) and stop when there is no more overlapping AR objects in the next time step (e.g., t+[n+1] in Figure 5),

or when combination/division/deformation occurs (in this case, the overlapping AR object in the next time step will be marked as a type II/III/IV origin).

Note that the origin and termination of AR event may not necessarily be the "true" start and end of the strong and persistent IVT. The identified life cycle may miss or partly miss the developing or decaying time steps due to strict IVT threshold (exceeding 85th percentile) in AR condition detection. It is also worth noting that the algorithm proceeds under the assumption that the AR objects overlap in consecutive time steps. In this study, only the AR objects that persist for at least 12 hrs after their origins are retained. By this process, we neglect the very short-lived AR events. The identified AR events are archived respectively in sequential time order.

The algorithm tracks the life cycle of AR event by defining its origin, termination, and lifetime. The position (longitude and latitude) of AR object at each iteration step is determined by the centroid of IVT, which is calculated as

$$\bar{x} = \frac{\sum_{1}^{n} x_i m_i}{\sum_{1}^{n} m_i},\tag{3}$$

$$\overline{y} = \frac{\sum_{i=1}^{n} y_i m_i}{\sum_{i=1}^{n} m_i},\tag{4}$$

where \bar{x} and \bar{y} are the longitude and latitude of the IVT centroid; x_i and y_i are the longitude and latitude of the i^{th} grid of AR object; m_i is area-weighted IVT of i^{th} grid; n is total number of grids within the AR object. We define the line connecting these positions as track of AR objects (hereafter, AR track). For example, Figure 1b shows the recorded AR track (yellow line). The two black diamonds (Figure 1b) denote the origin and termination positions of AR track. The centroid of IVT may be located outside of the AR object when the shape of AR object is nonconvex (e.g., the red diamond mark corresponds to the blue object in Figure 1b).

2.2.3. Resolution Sensitivity

The sensitivities of the tracking algorithm to spatial and temporal resolutions are assessed. By comparing the

Centroid of IVT

Lifetime

t-1

t t+1

t+2
...

Urigin

Termination

Life cycle of AR event

Figure 5. Life cycle of atmospheric river event with type I origin.

detected AR objects using 1.5° and 2.5° ERA-Interim, GW15 found that coarser spatial resolution smooths the IVT field, so the detected AR objects are overall wider than those of higher resolution. Figure 6 shows the overlapping ratios of AR objects using ERA-Interim data with coarser spatial resolutions (1.5° versus 2.5° in 6-hourly). Our results suggest that the distribution of overlapping ratios does not change significantly as spatial resolution decreases to coarser resolutions (from 1° to 2.5°, Figure 6). Although the number of AR objects having 0% overlapping ratios drops with coarser resolution, the relative ratio to total remains similar (about 20%) due to the overall decrease in the counts of AR objects (leftmost bar in Figure 6). The

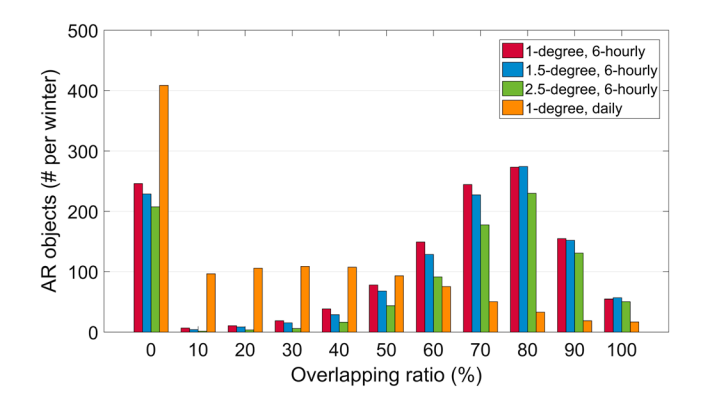


Figure 6. Same as Figure 3b but with data of various horizontal and temporal resolutions. Note that the distribution of 1°daily data is scaled by 4.

average number of total AR events (including 4 types) over the North Pacific is 102 for 1°, 96 for 1.5°, and 90 for 2.5°.

We also compare the sensitivity to temporal resolution using 1° daily IVT, which is the average of 6-hourly data (orange bars in Figure 6). Since temporal steps are reduced by a factor of 4 with daily frequency, the distribution of overlapping ratios is scaled by 4 for a fair comparison. Comparing with 6-hourly IVT over the North Pacific, the number (relative ratio to total AR objects) of AR objects with 0% overlapping ratio of daily IVT increases from 244 (19%) to 408 (37%) per winter, and the nonzero peak of overlapping ratios shifts from 70% to 30% (Figure 6). The number of identified AR events drops about 50% from 6-hourly (102 AR events) to daily (47 AR events) IVT. Overall, the tracking algorithm is more sensitive to temporal than spatial resolution.

3. Results

3.1. AR Life Cycle: Origin, Termination, and Track

We focus on the AR events originating over the North Pacific (0°N–90°N, 120°E–125°W). Figure 7a shows the climatological origin frequency (number per winter) integrating the four origin types. Due to the abundant moisture at low latitudes, most of the AR events start from the subtropics between 20°N and 35°N with high occurrence frequency along 25°N over the Northwest Pacific between 130°E and 170°E (dash box in Figure 7 a), which agrees with previous study (Sellars et al., 2017). The high origin frequency over the subtropical Northwest Pacific may be associated with cyclone activity (Cordeira et al., 2013). Another high origin

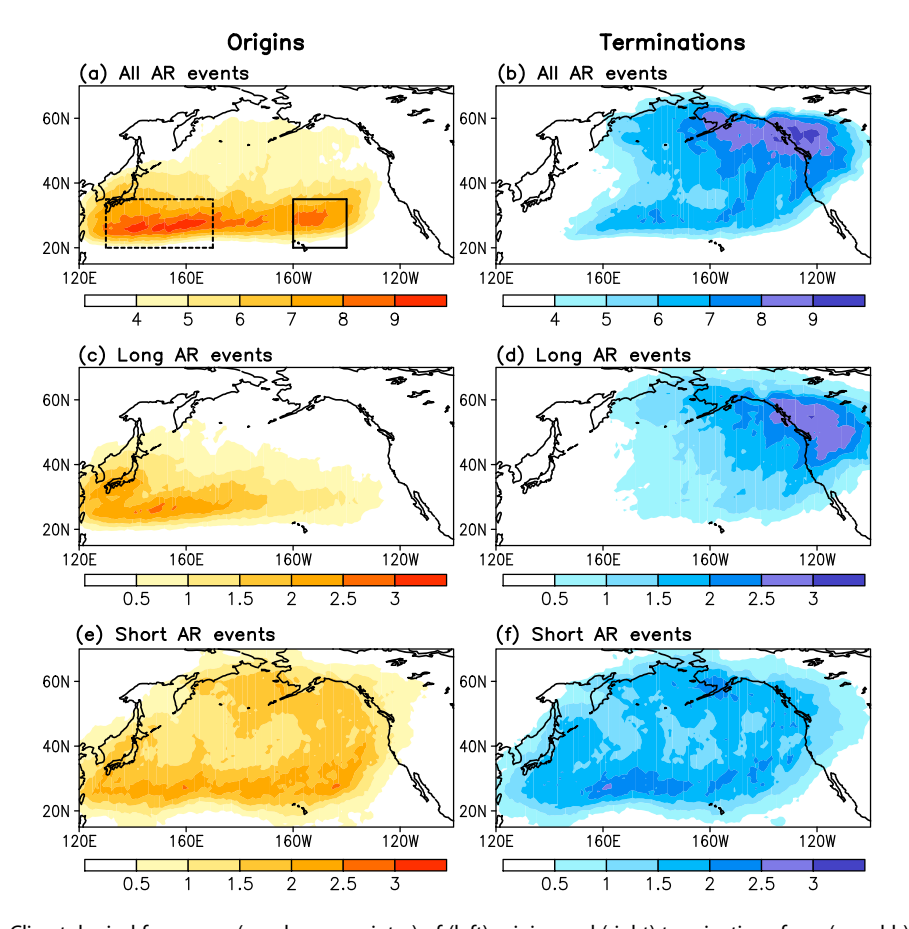


Figure 7. Climatological frequency (number per winter) of (left) origins and (right) terminations from (a and b) all atmospheric river (AR) events, (c and d) long AR events, and (e and f) short AR events.

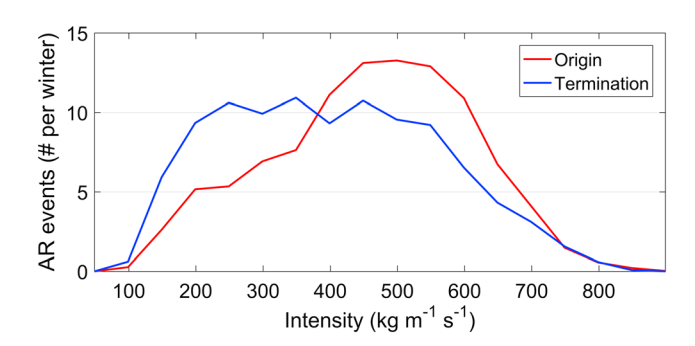


Figure 8. Distribution of intensities for origins and terminations.

frequency region appears over the Northeast Pacific (solid box [20°N–35°N, 140°W–160°W] in Figure 7a). This high origin frequency region corresponds to the features described as "Pineapple Express" events, which describes the strong and persistent IVT from the Hawaiian Islands (about 19°N, 150°W) to the west coast of North America.

The regions of high termination frequency shift roughly 20° north and 20–40° east of origins (Figure 7b), which implies that the propagation of AR objects is mainly northeastward. Most of the AR events terminate over the Central and Northeast Pacific, especially over western North America. Although the origins are packed in the subtropics, the terminations spread over the North Pacific because of the changes in propagation, lifetime, and intensity in the life cycles. The zonally distributed high termination fre-

quency at 30°N is related to AR events with relatively shorter lifetime (Figures 7b and 7f, discussed in section 3.2).

Figure 8 shows the 38-season averaged intensity distribution of origins and terminations. The intensity is calculated as domain-averaged IVT of AR object. The intensities of origins concentrate between 400 and 600 kg m $^{-1}$ s $^{-1}$, with a mean value of 460.8 kg m $^{-1}$ s $^{-1}$. The intensities of terminations spread widely between 250 and 500 kg m $^{-1}$ s $^{-1}$ with a mean of 403.0 kg m $^{-1}$ s $^{-1}$. The mean origin intensity is stronger than mean termination intensity at 95% significance level, using a t test. The probability of intensities being less than 380 kg m $^{-1}$ s $^{-1}$ is significantly higher for terminations (~65%) than the origins (~35%) because the AR events generally terminate at higher latitudes with less moisture. However, about 50% of AR events terminate with intensities stronger than 400 kg m $^{-1}$ s $^{-1}$. The location and characteristics of such terminations with strong intensities will be further studied.

The AR track (yellow line in Figure 1b) illustrates the pathway of AR objects from origin to termination. Figure 9 shows the climatological AR track density over the North Pacific in 6-hourly time step from November to March. For displaying purpose, the AR track density is interpolated into 5°×5° grid to reduce noise. Note that the AR track density shows the mean track of AR events, which is distinguished from AR frequency (e.g., Figure 1c). The distribution of AR track density agrees with Payne and Magnusdottir (2014), who showed the tracks of AR events determined by different criteria. The mean AR track density distributes zonally across the North Pacific and tilts northeastwardly. High AR track density mainly appears over the Central and Northeast Pacific between 30°N and 40°N, indicating the major pathway of AR objects. The spread of AR track density over the west coast of North America implies the vast range in the landfalling latitudes of AR events (Figure 9).

3.2. Long Versus Short AR Events

Previous studies define AR duration using the number of hours that an AR condition sustains over a given grid cell, which represents the potential AR impact on a given location (Guan & Waliser, 2015; Payne & Magnusdottir, 2016; Ralph et al., 2013; Rutz et al., 2014; Sellars et al., 2017). Here by taking advantage of the tracking algorithm, we define the lifetime (i.e., duration of an AR event) by adding up the total hours

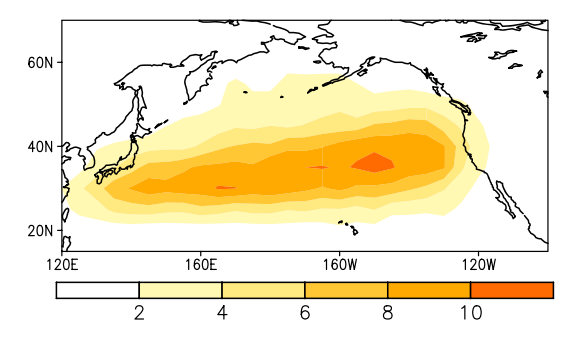


Figure 9. Climatological atmospheric river (AR) tracks density (number of AR tracks per winter) interpolated to $5^{\circ}\times5^{\circ}$ grid.

((time steps - 1) × 6 hrs) between origin and termination defined by Step II (Figure 5). Figure 10 shows the 38-season averaged distribution of AR lifetime. Each bin includes the left edge but not the right edge. For example, the first bin from the left indicates that about 33% of total AR events last in the range of ≥12 and <24 hrs. The mean lifetime of all identified AR events is about 42 hrs. We compare the characteristics of two groups of AR events based on lifetime (Figure 10): short AR events (<24 hrs, roughly the 30th percentile) and long AR events (>72 hrs, the 85th percentile). The reason we choose the 30th percentile of lifetime is that the minimum lifetime among all AR events is 18 hrs based on 6-hourly time interval, which is about 30% of the total AR events. Meanwhile, 72 hrs marks the 85th percentile of lifetime, which is a reasonable cutoff for long AR events.

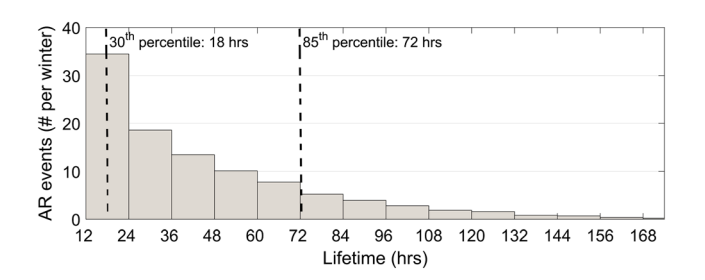


Figure 10. The number of atmospheric river events as a function of lifetime (hrs). The dash lines mark the 30th and 85th percentiles.

The origin and termination frequency of long AR events are investigated (Figures 7c and 7d). High origin frequency of long AR events assembles over the Northwest Pacific at 25°N (Figure 7c), which takes up about 30% of total origin frequency over the Northwest Pacific (Figure 7a). High termination frequency of long AR events is located over the coastal and inland of western North America (Figure 7d), which occupies up to 40% of total termination frequency over North America (Figure 7b). For short AR events, the origin frequency spreads over the entire North Pacific with high frequency along the subtropics (Figure 7e). Over the Northeast Pacific, the high origin frequency at the subtropics shows a southwest-northeast orientation between

25°N–45°N and 130°W–150°W, which coincides with the pathway of "Pineapple Express" (Figure 7a). The terminations of short AR events are generally located close to their origins due to the short lifetime (Figure 7f). The origin frequency of short AR events is relatively higher adjacent to the west coast (Figure 7e). These short AR events can landfall over North America (Figure 7f), which explains about 15–20% of total termination frequency over North America (Figure 7b).

By comparing the distances between origins and terminations of long and short AR events, we hypothesize that the traveled distance of an AR event is positively correlated with its lifetime. To test the hypothesis, we define the traveled distance of AR event as the sum of great circle distance between two adjacent positions in the AR track (e.g., black dots in Figure 1b). The average traveled distance of all detected AR events over the North Pacific is about 2,500 km (Figure 11a), which is around 6% of Earth's circumference. The distributions of long and short AR events are 95% significantly different from the total distribution based on a t test. The average traveled distance of long AR events is 6,000 km (Figure 11a), which takes up to 15% of Earth's circumference. The mean traveled distance of short AR events is 860 km, which is nearly one-seventh of that of long AR events. As expected, with more than 3,800 AR events over the North Pacific during 38 winters, a strong relation between traveled distance and lifetime is shown such that the traveled distance increases proportionally with longer lifetimes, with a correlation coefficient of 0.91.

The propagation speed in AR events is defined as the averaged moving speed of AR objects of all time steps

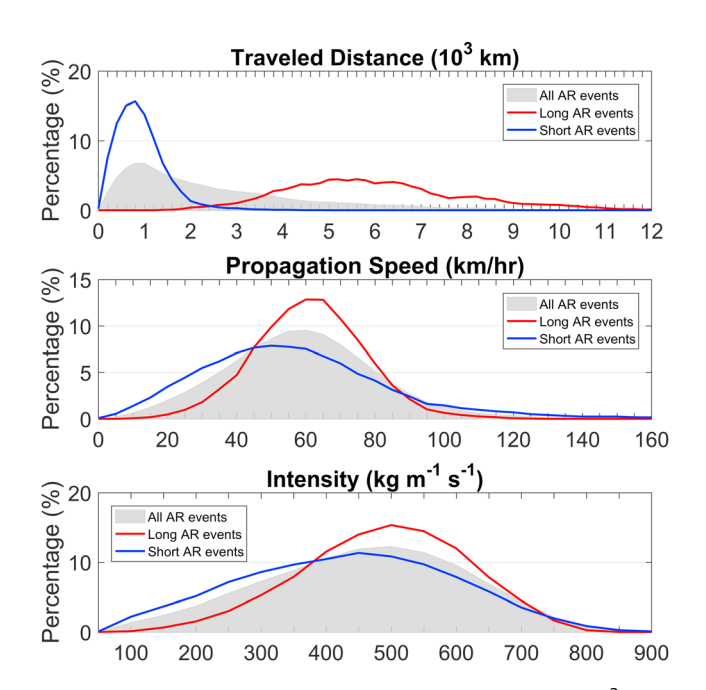


Figure 11. Percentage distributions of the (a) traveled distance (10^3 km) , (b) propagation speed (km/hr), and (c) intensity (kg m⁻¹ s⁻¹) for all atmospheric river (AR) events (gray shading), long AR events (red line), and short AR events (blue line).

within one AR event. The propagation speed is calculated by dividing the traveled distance with lifetime (Figure 11b). The average propagation speed of all AR events is about 60 km/hr. The propagation speeds are comparable between long AR events (61 km/hr) and short AR events (59 km/hr), although the standard deviation in the propagation speeds of short AR events (33 km/hr) is more than twice of those of long AR events (14 km/hr; Figure 11b). The probability of propagation speeds being less than 45 km/hr increases in short AR events (30%) comparing to long AR events (10%)

We define the intensity of an AR event as the average intensity of AR objects of all time steps within one AR event. The intensity distributions of all, long and short AR events are 95% significantly different from one another based on a t test (Figure 11c). The average intensity of all AR events over the North Pacific is 458 kg m $^{-1}$ s $^{-1}$. The long AR events show a compact distribution of intensities with a mean of 489 kg m $^{-1}$ s $^{-1}$, which is 95% significantly stronger than the mean intensity of short AR events (431 kg m $^{-1}$ s $^{-1}$). However, no linear relationship is found between intensity and lifetime.

3.3. Accumulated AR Intensity Index

To represent the overall activity of the North Pacific AR events during winter, we develop a new index called the ARI index. The concept is similar to the Accumulated Cyclone Energy index that represents the overall tropical cyclone activity of a certain period (Bell et al., 2000). The ARI index employs

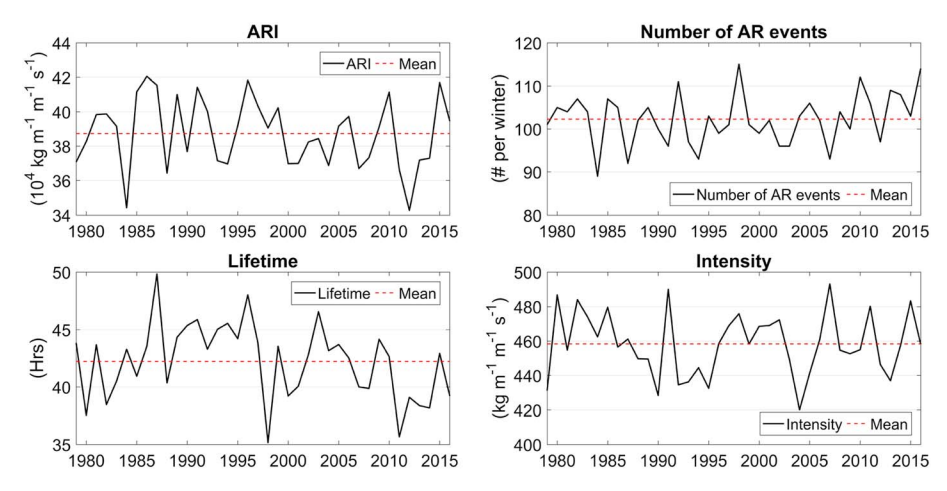


Figure 12. Year-to-year variation of (a) accumulated atmospheric river (AR) intensity index ($10^4 \text{ kg m}^{-1} \text{ s}^{-1}$); (b) number of AR events (number per winter); (c) seasonal mean lifetime (hrs); (d) seasonal mean intensity (kg m⁻¹ s⁻¹) in the North Pacific during November–March from 1979/1980 to 2016/2017.

the number, lifetime, and intensities of AR events recorded by the new tracking algorithm. The ARI index is defined as

$$\sum_{i=1}^{i=N} \sum_{t=1}^{t=T_i} [IVT(t)]_i, \tag{5}$$

where N is the number of AR events of each winter season; T_i is the number of time steps of the ith AR event (e.g., $T_i = n$ in Figure 5), which represents the lifetime; and $[IVT(t)]_i$ is the intensity of AR object at time step t of the ith AR event. The unit of ARI index is 10^4 kg m⁻¹ s⁻¹.

Figure 12a shows the year-to-year change of seasonal ARI index during the winter of 1979/1980 to 2016/2017 over the North Pacific. The mean value of ARI index is 38.7×10^4 kg m⁻¹ s⁻¹. Multiple factors can affect the interannual change of ARI index. To compare the relative contributions, time series of the number of AR events, seasonal mean lifetime, and seasonal mean intensity are calculated (Figures 12b–12d). The interannual variability of the number of AR events is not significantly related to the ARI index, which has a correlation coefficient of 0.30 (Figure 12b). The seasonal mean lifetime is the dominant factor in the interannual change of ARI. The correlation coefficient of mean lifetime against ARI is 0.40, which exceeds the 95% significance level of a t test (Figure 12c). Interestingly, the number of AR events and mean lifetime are significantly anticorrelated, with a correlation coefficient of -0.54. This indicates that during winter, the mean lifetime tends to decrease with increasing number of AR events. Finally, the mean intensity shows the least influence on ARI, with a correlation of 0.23 (Figure 12d). Overall, the interannual variability of ARI is modulated mainly by the seasonal mean lifetime. The interannual variability of the overall AR activity and the contribution of each factor will be explored in depth in future study.

4. Summary and Discussion

An object-based tracking algorithm is developed in this study to identify AR events and track their life cycles. The AR event contains a series of spatiotemporally connected AR objects of contiguous time steps. The new tracking algorithm can record the life cycle of AR event including its origin and termination, track, lifetime, intensity, traveled distance, and propagation speed. This tracking algorithm is applicable to gridded reanalysis products or model outputs and suitable for different AR detection methods. Results from the tracking algorithm show that the North Pacific AR events mostly start between 20°N and 40°N and terminate over high latitudes of 40°N–60°N, including western North America. The climatological AR tracks display a zonally elongated pathway of AR objects. Most of the long AR events start from the subtropics and make landfall along the west coast of North America, extending inland, while the origins of short AR events spread over the North Pacific. The propagation speeds in long and short AR events are comparable. The traveled distance of an AR event increases proportionally with a longer lifetime. On average, long AR events travel 7 times



longer in distance with stronger intensity than short AR events. Finally, the ARI index is developed to represent the AR activity over a given region and during a certain period, which includes the number, lifetime, and intensities of AR events. A high ARI index may come from frequent AR events or strong and persistent AR events during a season. However, it remains unclear that how these components are linked with each other and how each component responses to various climate modes.

We will further examine the interannual variability of the AR life cycles and underlying mechanisms and their local impacts. For example, with the new tracking algorithm, it is feasible to sort out specific AR events to study their unique synoptic features and possible mechanisms, which has implications for improving the understanding of the causes and processes of local hydrological events. Moreover, the tracking algorithm can be applied to climate model output for a process-based model evaluation, and to forecast output to assess predictability and skills of ARs, and to global warming scenarios to provide detailed characteristics of AR life cycles associated with climate change.

Acknowledgments

Constructive and valuable comments from three anonymous reviewers are greatly appreciated. This study was supported by NSF grant AGS-1652289 and KMA R&D program grant KMI2018-03110. The sources of data used in this study are http://apps.ecmwf.int/datasets/data/interim-full-daily/levtype=pl/ for ERA-Interim reanalysis. The Guan and Waliser (2015)'s AR detection code (in Matlab) can be obtained from https://goo.gl/forms/ZAOKUihOEtjWk3dh2

References

- Baggett, C. F., Barnes, E. A., Maloney, E. D., & Mundhenk, B. D. (2017). Advancing atmospheric river forecasts into subseasonal-to-seasonal time scales. *Geophysical Research Letters*, 44, 7528–7536. https://doi.org/10.1002/2017GL074434
- Bao, J. W., Michelson, S. A., Neiman, P. J., Ralph, F. M., & Wilczak, J. M. (2006). Interpretation of enhanced integrated water vapor bands associated with extratropical cyclones: Their formation and connection to tropical moisture. *Monthly Weather Review*, 134(4), 1063–1080. https://doi.org/10.1175/Mwr3123.1
- Bell, G. D., Halpert, M. S., Schnell, R. C., Higgins, R. W., Lawrimore, J., Kousky, V. E., Tinker, R., et al. (2000). Climate assessment for 1999. Bulletin of the American Meteorological Society, 81(6), S1–S50. https://doi.org/10.1175/1520-0477(2000)81[s1:CAF]2.0.CO;2
- Cordeira, J. M., Ralph, F. M., & Moore, B. J. (2013). The development and evolution of two atmospheric rivers in proximity to Western North Pacific tropical cyclones in October 2010. *Monthly Weather Review, 141*(12), 4234–4255. https://doi.org/10.1175/Mwr-D-13-000191
- Dee, D. P., Uppala, S. M., Simmons, A. J., Berrisford, P., Poli, P., Kobayashi, S., Andrae, U., et al. (2011). The ERA-Interim reanalysis: Configuration and performance of the data assimilation system. *Quarterly Journal of the Royal Meteorological Society*, 137(656), 553–597. https://doi.org/10.1002/gi.828
- DeFlorio, M. J., Waliser, D. E., Guan, B., Lavers, D. A., Ralph, F. M., & Vitart, F. (2018). Global assessment of atmospheric river prediction skill. Journal of Hydrometeorology, 19(2), 409–426. https://doi.org/10.1175/Jhm-D-17-0135.1
- DeFlorio, M. J., Waliser, D. E., Guan, B., Ralph, F. M., & Vitart, F. (2018). Global evaluation of atmospheric river subseasonal prediction skill. Climate Dynamics, 1–22. https://doi.org/10.1007/s00382-018-4309-x
- Dettinger, M. D. (2013). Atmospheric rivers as drought busters on the US west coast. *Journal of Hydrometeorology*, 14(6), 1721–1732. https://doi.org/10.1175/Jhm-D-13-02.1
- Dettinger, M. D., Ralph, F. M., Das, T., Neiman, P. J., & Cayan, D. R. (2011). Atmospheric rivers, floods and the water resources of California. *Water*, 3(2), 445–478. https://doi.org/10.3390/w3020445
- Guan, B., Molotch, N. P., Waliser, D. E., Fetzer, E. J., & Neiman, P. J. (2010). Extreme snowfall events linked to atmospheric rivers and surface air temperature via satellite measurements. *Geophysical Research Letters*, 37, L20401. https://doi.org/10.1029/2010GL044696
- Guan, B., Molotch, N. P., Waliser, D. E., Fetzer, E. J., & Neiman, P. J. (2013). The 2010/2011 snow season in California's Sierra Nevada: Role of atmospheric rivers and modes of large-scale variability. *Water Resources Research*, 49, 6731–6743. https://doi.org/10.1002/wrcr.20537
- Guan, B., & Waliser, D. E. (2015). Detection of atmospheric rivers: Evaluation and application of an algorithm for global studies. *Journal of Geophysical Research: Atmospheres*, 120, 12514–12535. https://doi.org/10.1002/2015JD024257
- Guan, B., & Waliser, D. E. (2017). Atmospheric rivers in 20 year weather and climate simulations: A multimodel, global evaluation. *Journal of Geophysical Research: Atmospheres, 122*, 5556–5581. https://doi.org/10.1002/2016JD026174
- Kim, H. M., Zhou, Y., & Alexander, M. A. (2017). Changes in atmospheric rivers and moisture transport over the Northeast Pacific and western North America in response to ENSO diversity. Climate Dynamics, 1–14. https://doi.org/10.1007/s00382-017-3598-9
- Knippertz, P., & Wernli, H. (2010). A Lagrangian climatology of tropical moisture exports to the Northern Hemispheric extratropics. *Journal of Climate*, 23(4), 987–1003. https://doi.org/10.1175/2009JCli3333.1
- Mundhenk, B. D., Barnes, E. A., & Maloney, E. D. (2016). All-season climatology and variability of atmospheric river frequencies over the North Pacific. *Journal of Climate*, 29(13), 4885–4903. https://doi.org/10.1175/Jcli-D-15-0655.1
- Mundhenk, B. D., Barnes, E. A., Maloney, E. D., & Baggett, C. F. (2018). Skillful empirical subseasonal prediction of landfalling atmospheric river activity using the Madden-Julian oscillation and quasi-biennial oscillation. NPJ Climate and Atmospheric Science, 1(1), 20177. https://doi.org/10.1038/s41612-017-0008-2
- Mundhenk, B. D., Barnes, E. A., Maloney, E. D., & Nardi, K. M. (2016). Modulation of atmospheric rivers near Alaska and the US West Coast by Northeast Pacific height anomalies. *Journal of Geophysical Research: Atmospheres, 121*, 12,751–12,765. https://doi.org/10.1002/2016id025350
- Neiman, P. J., Ralph, F. M., Moore, B. J., Hughes, M., Mahoney, K. M., Cordeira, J. M., & Dettinger, M. D. (2013). The landfall and inland penetration of a flood-producing atmospheric river in Arizona. Part I: Observed synoptic-scale, orographic, and hydrometeorological characteristics. *Journal of Hydrometeorology*, 14(2), 460–484. https://doi.org/10.1175/Jhm-D-12-0101.1
- Neiman, P. J., Ralph, F. M., Wick, G. A., Lundquist, J. D., & Dettinger, M. D. (2008). Meteorological characteristics and overland precipitation impacts of atmospheric rivers affecting the West Coast of North America based on eight years of SSM/I satellite observations. *Journal of Hydrometeorology*, 9(1), 22–47. https://doi.org/10.1175/2007jhm855.1
- Payne, A. E., & Magnusdottir, G. (2014). Dynamics of landfalling atmospheric rivers over the North Pacific in 30 years of MERRA reanalysis. Journal of Climate, 27(18), 7133–7150. https://doi.org/10.1175/Jcli-D-14-00034.1
- Payne, A. E., & Magnusdottir, G. (2016). Persistent landfalling atmospheric rivers over the west coast of North America. *Journal of Geophysical Research: Atmospheres*, 121, 13,287–13,300. https://doi.org/10.1002/2016JD025549



- Ralph, F. M., Coleman, T., Neiman, P. J., Zamora, R. J., & Dettinger, M. D. (2013). Observed impacts of duration and seasonality of atmospheric-river landfalls on soil moisture and runoff in coastal northern California. *Journal of Hydrometeorology*, 14(2), 443–459. https://doi.org/10.1175/Jhm-D-12-076.1
- Ralph, F. M., Iacobellis, S. F., Neiman, P. J., Cordeira, J. M., Spackman, J. R., Waliser, D. E., Wick, G. A., et al. (2017). Dropsonde observations of total integrated water vapor transport within North Pacific atmospheric rivers. *Journal of Hydrometeorology*, *18*(9), 2577–2596. https://doi.org/10.1175/Jhm-D-17-0036.1
- Ralph, F. M., Neiman, P. J., Wick, G. A., Gutman, S. I., Dettinger, M. D., Cayan, D. R., & White, A. B. (2006). Flooding on California's Russian River: Role of atmospheric rivers. *Geophysical Research Letters*, 33, L13801. https://doi.org/10.1029/2006GL026689
- Ramos, A. M., Nieto, R., Tome, R., Gimeno, L., Trigo, R. M., Liberato, M. L. R., & Lavers, D. A. (2016). Atmospheric rivers moisture sources from a Lagrangian perspective. *Earth System Dynamics*, 7(2), 371–384. https://doi.org/10.5194/esd-7-371-2016
- Rutz, J. J., Steenburgh, W. J., & Ralph, F. M. (2014). Climatological characteristics of atmospheric rivers and their inland penetration over the Western United States. *Monthly Weather Review*, 142(2), 905–921. https://doi.org/10.1175/Mwr-D-13-00168.1
- Rutz, J. J., Steenburgh, W. J., & Ralph, F. M. (2015). The inland penetration of atmospheric rivers over Western North America: A Lagrangian analysis. *Monthly Weather Review*, 143(5), 1924–1944. https://doi.org/10.1175/Mwr-D-14-00288.1
- Ryoo, J. M., Waliser, D. E., Waugh, D. W., Wong, S., Fetzer, E. J., & Fung, I. (2015). Classification of atmospheric river events on the US West Coast using a trajectory model. *Journal of Geophysical Research: Atmospheres, 120,* 3007–3028. https://doi.org/10.1002/2014jd022023
- Sellars, S. L., Gao, X. G., & Sorooshian, S. (2015). An object-oriented approach to investigate impacts of climate oscillations on precipitation: A Western United States case study. *Journal of Hydrometeorology*, 16(2), 830–842. https://doi.org/10.1175/Jhm-D-14-0101.1
- Sellars, S. L., Kawzenuk, B., Nguyen, P., Ralph, F. M., & Sorooshian, S. (2017). Genesis, pathways, and terminations of intense global water vapor transport in association with large-scale climate patterns. *Geophysical Research Letters*, 44, 12,465–12,475. https://doi.org/10.1002/
- Shields, C. A., Rutz, J. J., Leung, L. Y., Ralph, F. M., Wehner, M., Kawzenuk, B., Lora, J. M., et al. (2018). Atmospheric River Tracking Method Intercomparison Project (ARTMIP): Project goals and experimental design. *Geoscientific Model Development Discussion*, 2018, 1–55. https://doi.org/10.5194/gmd-2017-295
- Sodemann, H., & Stohl, A. (2013). Moisture origin and meridional transport in atmospheric rivers and their association with multiple cyclones. Monthly Weather Review, 141(8), 2850–2868. https://doi.org/10.1175/Mwr-D-12-00256.1
- Stohl, A., Forster, C., & Sodemann, H. (2008). Remote sources of water vapor forming precipitation on the Norwegian west coast at 60 degrees N—A tale of hurricanes and an atmospheric river. *Journal of Geophysical Research*, 113, D05102. https://doi.org/10.1029/2007JD009006
- Stohl, A., & James, P. (2004). A Lagrangian analysis of the atmospheric branch of the global water cycle. Part I: Method description, validation, and demonstration for the August 2002 flooding in central Europe. *Journal of Hydrometeorology*, *5*(4), 656–678. https://doi.org/10.1175/1525-7541(2004)005<0656:Alaota>2.0.Co;2
- Waliser, D. E., & Guan, B. (2017). Extreme winds and precipitation during landfall of atmospheric rivers. *Nature Geoscience*, 10(3), 179–U183. https://doi.org/10.1038/Ngeo2894
- Zhou, Y., & Kim, H. M. (2017). Prediction of atmospheric rivers over the North Pacific and its connection to ENSO in the North American multimodel ensemble (NMME). Climate Dynamics, 51(5-6), 1623–1637. https://doi.org/10.1007/s00382-017-3973-6
- Zhu, Y., & Newell, R. E. (1994). Atmospheric rivers and bombs. *Geophysical Research Letters*, 21(18), 1999–2002. https://doi.org/10.1029/94GI.01710
- Zhu, Y., & Newell, R. E. (1998). A proposed algorithm for moisture fluxes from atmospheric rivers. *Monthly Weather Review*, 126(3), 725–735. https://doi.org/10.1175/1520-0493(1998)126<0725:Apafmf>2.0.Co;2